Turbulence Measurements on a Wing-Fuselage Junction Model for CFD Validation

Michael Kegerise, Dan Neuhart, and Christopher Rumsey

NASA Langley Research Center
1A East Reid Street, MS 170
Hampton, VA 23681
UNITED STATES

michael.a.kegerise@nasa.gov

ABSTRACT

Current turbulence models, such as those employed in Reynolds-averaged Navier-Stokes CFD, are unable to reliably predict the onset and extent of the three-dimensional separated flow that typically occurs in wing-fuselage junctions. To critically assess, as well as to improve upon, existing turbulence models, experimental validation-quality flowfield data in the junction region is needed. To that end, NASA has developed a CFD validation experiment for a generic full-span wing-fuselage junction model at subsonic conditions. In this paper, we present and discuss sample results from this effort, with a focus on turbulence measurements in the separated corner flow of the wing-fuselage junction that were obtained with an internally mounted laser Doppler velocimetry (LDV) system. In addition, sample comparisons between the flowfield measurements and representative CFD of our test case are presented and here, we highlight some of the key discrepancies.

1.0 INTRODUCTION

Junction flows, such as those formed around a wing-fuselage or a wing-pylon intersection, are common features of practically all civil and military aircraft. Since these flows typically exhibit regions of flow separation that can adversely impact aircraft performance, there is a strong desire to accurately predict the behavior associated with them. For wing-fuselage junction flows in particular, the flow is often observed to separate in the corner-flow region near the wing trailing edge. However, the turbulence models currently employed in Reynolds-averaged Navier-Stokes CFD are unable to reliably predict the onset and extent of this separated corner flow. For example, CFD computations at past Drag Prediction Workshops have displayed large variations in the predictions of separation, skin friction, and pressure in the corner-flow region near the wing trailing edge [1]. To critically assess our existing turbulence models, as well as to improve upon them, experimental validation-quality flowfield data in the junction region is needed. To address that, NASA has developed a CFD validation experiment for a generic full-span wing-fuselage junction model at subsonic conditions. Rumsey *et al.* have previously reported on the detailed goals of this effort and has provided a history of its development [2, 3]. The ultimate goal of this experiment is to provide a publicly-available high-quality flowfield and surface data set with quantified boundary conditions, geometry, and measurement uncertainties. This data set should be suitable for use in CFD workshop environments and will help CFD practitioners validate and improve their predictive capabilities for turbulent separated corner flows.

In late 2017 and early 2018, the junction flow CFD validation experiment was conducted in the NASA Langley 14- by 22-Foot Subsonic Tunnel (14x22) and for that first test entry, the junction model was configured with a truncated DLR-F6 wing geometry. The primary objective was to perform flowfield measurements in the

trailing-edge corner region of the wing-fuselage junction with an internally mounted laser Doppler velocimetry (LDV) system. The LDV system provided measurements from which all three velocity components, all six independent components of the Reynolds-stress tensor, and all ten independent components of the velocity triple products were calculated. A second internally mounted LDV system was alternately used to measure the flowfield in the leading-edge region of the wing and to measure the incoming fuselage boundary layer well upstream of the leading edge. In addition to the flowfield measurements, static and dynamic pressures were measured at selected locations on the wings and fuselage of the model, infrared imaging was used to characterize boundary-layer transition, and oil flow was used to visualize the separated flow in the leading- and trailing-edge regions of the wing. An overview of this test entry was recently reported by Kegerise *et al.* [4] and more detailed documentation of the test entry can be found in a report by Kegerise and Neuhart [5]. The experimental data for this test entry can be obtained from the NASA Langley Turbulence Modeling Resource webpage[1].

Over the course of the test entry, a concerted effort was made to document the as-built, as-assembled, and as-tested geometry of the junction model using laser-based scanning techniques. The wind-tunnel test-section geometry was also documented and measurements of the tunnel wall pressures, diffuser pressures, and boundary-layer rake pressures were acquired during the test entry. The ultimate goal for this group of measurements was to provide documented geometry and boundary conditions so that an unambiguous comparison between CFD calculations and the experimental measurements can be made. The details of the test geometry and the boundary-condition data can also be found on the Turbulence Modeling Resource webpage.

In this paper, we present sample results from the junction flow CFD validation experiment, but limit them to the LDV measurements in the separated corner flow near the trailing-edge of the wing-fuselage junction. Sample profiles of the mean velocity, Reynolds stresses, and turbulent kinetic energy in this region of the flow, along with histograms of the velocity fluctuations, will be presented and discussed. In addition, we will present comparisons between the flowfield measurements and CFD calculations of our test case, and here, we will highlight some of the key discrepancies.

2.0   EXPERIMENTAL METHODS

2.1   Wind-Tunnel Facility

The experiment was performed in the NASA Langley 14- by 22-Foot Subsonic Tunnel, which is a closed-circuit, atmospheric-pressure wind tunnel capable of operating in an open, partially closed, or closed test-section mode. Raising and lowering the test section side walls and ceiling creates the various modes of tunnel geometry. Measurements for the CFD validation experiment were made in the closed test-section mode and in that case, the test section measures 4.42 m high and 6.63 m wide, with a maximum freestream velocity of 103 m/s. Flow conditioning is provided by a flow-straightening honeycomb, four square-mesh screens with a mesh count of 10 per inch and 64% open area, and a tunnel contraction ratio of 9 to 1. This arrangement achieves a low test-section turbulence intensity of between 0.07 and 0.08 percent at a dynamic pressure (q_∞) of 2.87 kPa—but that does vary somewhat with dynamic pressure and location in the test section [6]. Further details about the tunnel can be found in Gentry *et al.* [7].

Throughout all of the wind-tunnel runs, the tunnel controller held the chord Reynolds number of the model, Re_c, at a constant value of 2.4 million. Since the 14x22 does not have a temperature controller, the air temperature increased over the course of a given run and therefore, the velocity was increased accordingly to maintain a constant chord Reynolds number. In addition, there were substantial changes in the nominal air temperature

---

[1]https://turbmodels.larc.nasa.gov, Accessed: 2019-05-15

from day-to-day and over the course of the test entry due to prevailing outdoor conditions. As such, the nominal tunnel velocity was again adjusted to maintain the target chord Reynolds number. In general, the air temperature ranged from 275 to 308 K and the Mach number ranged from 0.175 to 0.205 over the course of the test entry.

2.2 Wing-Fuselage Junction Model

The model was a full-span wing-fuselage body fabricated from 6061–T6 aluminum. The overall length, height, and width of the fuselage was 4.839 m, 0.670 m, and 0.472 m, respectively, and the tip-to-tip wing span was 3.397 m. A port side view of the model installed in the 14x22 wind tunnel is shown in Fig. 1. The model was painted with a black lusterless polyurethane paint suitable for both infrared imaging and oil-flow visualizations on the model surface. The measured paint thickness was on the order of 254 to 330 μm.

The model was attached to a long sting that could be raised or lowered via a motorized sting mast to keep a reference point on the model near the center of the test section during a pitch-angle adjustment. The reference point was located 2.448 m from the model

Figure 1: Junction model installed in the NASA Langley 14- by 22-Foot Subsonic Tunnel.

nose tip (or approximately 5.4 m from the test-section entrance) and on the fuselage centerline. Pitch angles for the test ranged from $-10°$ to $10°$ in increments of $2.5°$. Generally, the nominal height of the reference point was midway between the floor and ceiling; however, for pitch angles of $-10°$ and $-7.5°$, that height could not be achieved due to geometrical constraints on the sting-mast height. As such, the height was reduced to approximately 1.79 m and 2.06 m above the floor, respectively, for those two angles. The model sting was also motorized to allow for adjustments of the model roll angle, and over the course of the test, roll angles of $0°$ and $180°$ were considered. The pitch and roll angles of the model were measured with a pair of accelerometer-based model-attitude sensors that were located inside the model fuselage, and both sensors had a measurement uncertainty of $\pm0.01°$.

The junction-model fuselage was built in two parts: the fuselage nose section and the fuselage main section. The port and starboard sides of both sections of the fuselage were designed to be flat so that flat instrumentation inserts and windows could be used. Both fuselage sections also had removable hatches on the top and bottom that provided access to the internal instrumentation. An exploded view of the fuselage main section is shown in Fig. 2. This section has four removable inserts located on the flat sections of the fuselage sidewalls. For the LDV measurements in particular, the port side of the main fuselage section was configured with thin (1 mm), anti-reflection coated, acrylic windows that provided optical access to the flowfield. One window insert was located upstream of the wing box and provided optical access to the leading-edge region of the wing, while the other window insert was located downstream of the wing box and provided optical access to the trailing-edge corner region of the wing-fuselage junction. In Fig. 2, the fuselage main section is shown with two LDV systems in place and these were mounted to bridge pieces located inside the main section.

The junction model was configured with truncated DLR-F6 wings that are characterized by a leading-edge sweep angle of $27.1°$, dihedral, wash-out twist toward the wing tip, and a planform break located 759 mm from

**Turbulence Measurements on a Wing-Fuselage Junction Model
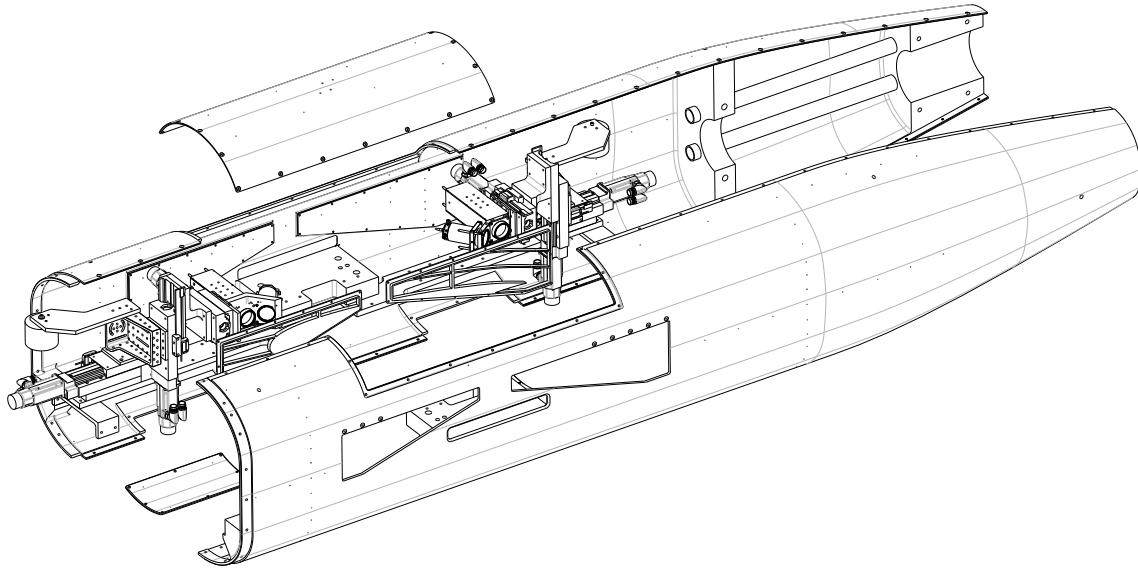for CFD Validation**

Figure 2: Exploded view of the fuselage main section assembly with LDV systems.

the fuselage sidewall. The planform break chord length for the wings was 557.17 mm and this was used as the reference length when calculating the chord Reynolds number. Using a removable insert around the leading-edge root region of the wing, the F6 wing could be configured with or without a leading-edge extension. This extension is simply a geometrical fairing intended to eliminate or minimize the development and influence of the horseshoe vortex that normally forms at the wing leading edge in the absence of the extension.

To ensure a turbulent boundary layer on the fuselage and the upper and lower surfaces of the wing, trip-dot arrays were used to fix the transition location. The trip dots were applied to the model with a commercially-produced trip-dot tape that is available in a range of heights. Specific details for the trip-dot geometry and the trip-dot placement on the fuselage and wings, including the results of transition characterization via infrared imaging, can be found in Kegerise and Neuhart [5].

2.3 Laser Doppler Velocimetry Measurements

As indicated earlier, the focus of this paper is on the LDV measurements made in the trailing-edge corner region of the wing-fuselage junction. For those measurements, a miniature laser Doppler velocimeter (LDV) probe was located inside the model, downstream of the fuselage main section wing box, and mounted to a three axis traverse system. With this setup, we were able to survey both upstream of and inside the separated corner flow. An image of the LDV system installed at the trailing-edge of the port wing is shown in Fig. 3.

The LDV system consisted of a photonics system that provided laser light to the LDV probe, a fiber-optic based probe head with off-axis receiving optics, a set of photomultipliers to detect Doppler bursts, and a data-acquisition computer with a high-speed A/D board and software for burst processing. The photonics system, which resided in a cart located outside the test section, consisted of the laser systems, discrete optics, and acousto-optic modulators (Bragg cells). Laser light for the system was proved by two continuous-wave diode-pumped solid-state lasers with a power output of 1 W. Both lasers provided laser light with a wavelength of 532 nm (green). Laser 1 was used to produce two beams (beam 1 with a frequency shift of 0 MHz and beam 2 with

a frequency shift of -200 MHz) that were delivered to the probe head via polarization-maintaining (PM) fibers. Laser 2 was used to produce three beams (beam 3 with a frequency shift of 0 MHz, beam 4 with a frequency shift of -80 MHz, and beam 5 with a frequency shift of 350 MHz) that were delivered to the probe head via PM fibers. All five single-mode PM fibers were bundled together in a stainless-steel armored conduit that was run from the photonics cart to the probe head in the junction model.

The LDV probe head, which is shown in Fig. 4a, was 22.8 cm long by 8 cm high by 7.7 cm wide. Laser light emitted from each of the PM fibers was collimated by a set of aspheric lenses that were arranged with the pattern shown in Fig. 4b. Note that for the measurement results presented in this paper, beams 6 and 7 (which provide a measure of particle position within the measurement volume) were not used. The beams emitted from the collimating lenses were then focused by a 90 mm focal length transmitting lens. The power of the laser beams emitted from the probe head were typically on the order of 100 mW. The five laser beams emitted from the probe head were crossed at their beam waists to form three measurement volumes: beams 1 and 2 with a frequency shift of -200 MHz, beams 3 and 4 with a frequency shift

Figure 3: LDV system located near the wing trailing edge.

of -80 MHz, and beams 3 and 5 with a frequency shift of 350 MHz. While an additional measurement volume was formed due to the interference between beams 4 and 5 (with a frequency shift of 430 MHz), the burst signals from that measurement volume are redundant and were discarded during the processing steps. For each of the measurement volumes, the nominal diameter and length was 140 μm and 960 μm, respectively. The measurement directions defined by these three measurement volumes are nonorthogonal and therefore, it was necessary to form a linear transformation to convert the measured velocity components to an orthogonal body-fixed coordinate system.
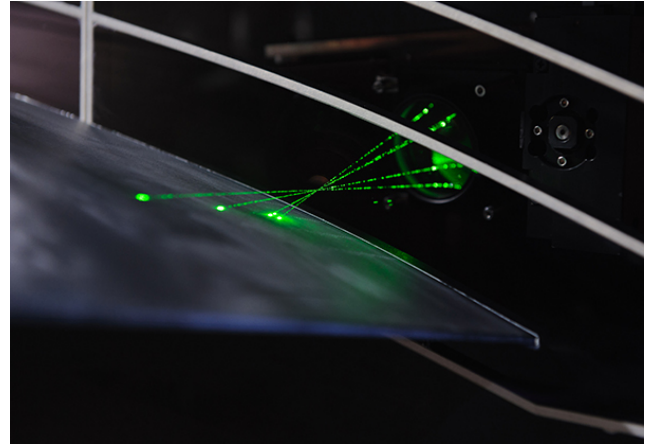
Scattered light from particles moving through the measurement volume was collected with a 110 mm focal-length lens oriented at approximately $35°$ to the optical axis of the probe head. Light collected with that lens was then focused onto a multimode fiber with a diameter of 105 μm. With this off-axis arrangement, the effective length of the measurement volumes was reduced to approximately 180 μm. The multimode receiving fiber was routed out of the junction model and test section to an enclosure that housed a photomultiplier for measurements of the burst signals carried by the receiving fiber. The amplified signal from the photomultiplier was then sent to the input of an 8 bit, 1 GS/s data-acquisition card. Burst detection was performed in the time domain and Doppler frequencies were extracted from the power-spectral densities of the sampled bursts signals. Specific details on the burst processing algorithm can be found in Lowe [8]. For the burst signals measured in the present study, three Doppler frequencies, associated with the three measurement volumes, were present. However, the frequency shift for each measurement volume was separated far enough apart in the frequency domain so that no signal ambiguity could occur for our flow conditions.

Seeding for the LDV measurements was provided by a smoke generator that uses a low-residue mineral oil and produces a narrow distribution of particle sizes with a nominal diameter of 0.94 μm. The smoke generator was placed in the wind tunnel settling chamber ahead of the honeycomb and it was necessary to run the generator continuously during a run to achieve adequate burst data rates. Depending on where the measurement volume was located in the flowfield, validated burst data rates on the order of 100 to 500 bursts/s

**Turbulence Measurements on a Wing-Fuselage Junction Model
for CFD Validation**
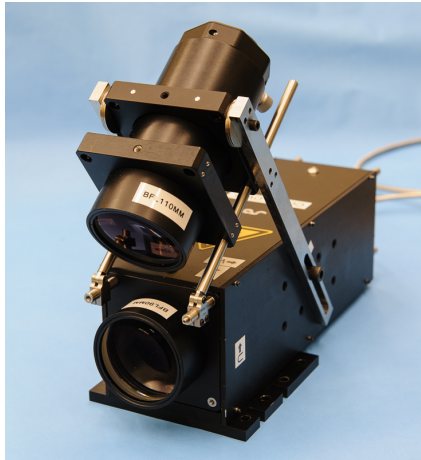
(a) Photograph of the LDV probe head with off-axis receiving optics.
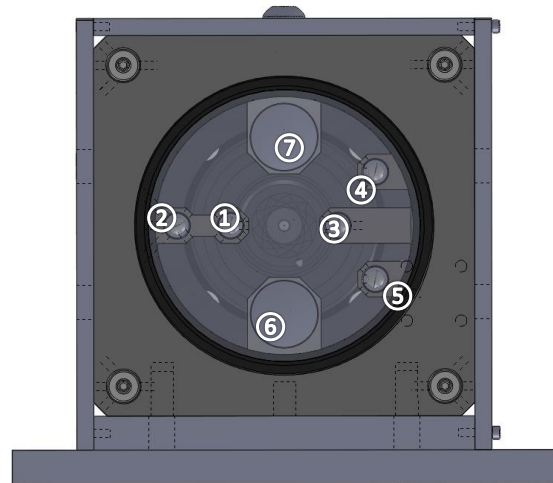
(b) Front view of the LDV probe head with annotated locations for the collimating lenses of laser beams 1–5.

Figure 4: Laser Doppler velocimetry probe head.

were achieved.

The measurement volume of the LDV probe was positioned in the flowfield with a three-axis traverse system. Traverse motion was performed in a body-fixed coordinate system with origin at the model nose tip and with coordinate directions as shown in Fig. 5. With the model at a pitch angle of $0°$ for example, the x-coordinate is positive in the downstream direction, the y-coordinate is positive toward the starboard wing tip, and the z-coordinate is positive in the upward direction. The x- and z-axis stages had a travel of 152.4 mm, a positional accuracy of 15 μm, and a bidirectional repeatability of ± 1 μm. The y-axis stage had a travel of 101.6 mm, a positional accuracy of 10 μm, and a bidirectional repeatability of ± 1 μm. The location of the LDV measurement volume relative to the fuselage window surface and to the wing surface was determined by the procedure described in Kegerise and Neuhart [5].

Figure 5: Body-fixed coordinate system for the junction model. The origin of the coordinate system is located at the model nose tip.

To determine the x-location for the flowfield measurements, the measurement volume was positioned relative to reference marks on the windows that were at known locations from the model nose tip.
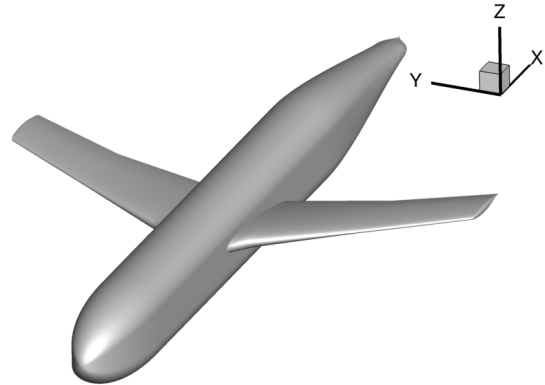
To process the LDV data, the unit vectors for each beam emitted by the LDV probe head were first measured using the digital-image-processing methodology described in Kegerise and Neuhart [5]. Using the measured unit vectors for each pair of beams that form a measurement volume, the measurement direction unit vectors and the measurement volume fringe spacings were calculated. After a fixed number of Doppler bursts were sampled, the measured Doppler frequencies from the three measurement volumes formed by the five green laser beams were used to calculate the nonorthogonal velocity components in the probe optical axes. The histograms

of those velocity components were then calculated and the histogram-clipping routine of Ölçmen and Simpson [9] was applied for removal of noise and outliers. The velocity components in the probe optical axes were then transformed to orthogonal velocity components in the body-fixed coordinate system. Histograms of those transformed velocity components were calculated and once again, the histogram-clipping routine was applied.

The processed velocity samples—which were sampled with random spacing in time—were then used to calculate several statistical moments. To account for velocity bias effects on the statistical moments, each sample was weighted by the particle transit time (or burst duration, which was recorded by the burst processor for each sample) through the measurement volume [10]. With this weighting factor, the mean x component of velocity was calculated as:

$$\overline{u} = \frac{\sum_i^N u_i \tau_i}{\sum_i^N \tau_i},\tag{1}$$

where τ_i is the transit time for a given sample i and N is the total number of samples. Similar equations were used to calculate the mean y component ($\overline{v}$) and z component ($\overline{w}$) of velocity. The Reynolds-stress components were calculated as:

$$\overline{u'v'} = \frac{\sum_i^N (u_i - \overline{u})(v_i - \overline{v})\tau_i}{\sum_i^N \tau_i},\tag{2}$$

with similar relations for the other five independent components: $\overline{u'u'}$, $\overline{v'v'}$, $\overline{w'w'}$, $\overline{u'w'}$, and $\overline{v'w'}$. The turbulent kinetic energy is defined as half the trace of the Reynolds stress tensor:

$$k = \frac{1}{2}\left(\overline{u'u'} + \overline{v'v'} + \overline{w'w'}\right),\tag{3}$$

and this is the mean kinetic energy per unit mass in the fluctuating velocity field. In Eq. 2, it is assumed that the u, v, and w velocities are available at the same instant in time and that was ensured by processing only coincident data.

At each measurement location in a flowfield survey, 30,000 samples were typically collected. For the data rates that were achieved with our LDV system (100 to 500 samples/s), many of the samples were statistically independent, being separated in time by at least two times the integral time scale. In general, the number of samples collected was more than sufficient to achieve well-converged statistical moments.

A detailed uncertainty analysis for statistical moments of the measured velocities is documented in Kegerise and Neuhart [5]. In summary, the systematic uncertainties in the statistical moments were estimated via direct Monte Carlo simulation [11] applied to the LDV data-reduction equations. The random uncertainties of the statistical moments that are due to sampling the random process associated with the turbulent flow were estimated with the formulas developed by Benedict and Gould [12]. The total uncertainty for the statistical moments was finally estimated as the root-sum-square of the systematic and random uncertainties. This uncertainty analysis was applied to each point in the flowfield surveys conducted over the course of the test entry. As such, the uncertainties in the statistical moments are unique to each point in the flowfield surveys.

3.0 NUMERICAL METHODS

Computations of the flowfield for our junction-model geometry were performed with the NASA FUN3D solver, which is an unstructured, three-dimensional, implicit, Navier-Stokes code that is nominally second order spatially accurate [13, 14]. Roe's flux splitting [15] was used for the calculation of the inviscid terms for all the results presented in this paper and flux limiters were not employed. Other details regarding the code can be found in the extensive bibliography that is accessible at the FUN3D website[2].

[2]NASA FUN3D CFD code, https://fun3d.larc.nasa.gov, Accessed: 2019-05-15.

The CFD computations presented in this paper were performed on the model (F6 wing with leading-edge extension) in free air. While some influence due to the tunnel walls was found in previous computations of the junction-model geometry [16], it is considered to be relatively minor for the quantities of interest in the current study. For the free-air computations, a far-field Riemann invariant boundary condition was imposed on the outer boundary, no-slip solid wall boundary conditions were applied on the junction-model geometry, and symmetry conditions were applied on the x–z plane (see Fig. 5). The Mach number was 0.189 and the chord Reynolds number (based on the planform break chord length) was 2.4 million. The computations were performed for angles of attack of $5°$ and $-2.5°$. Note, however, that the experimental measurements were made at geometric pitch angles of $5°$ and $-2.5°$, but due to the influence of the tunnel walls, the effective angles of attack for the measurements were slightly different.

Previous FUN3D results for the junction model geometry were obtained on a different set of grids [17]. Those grids were subsequently refined upstream of and within the wing-fuselage junction region for the computations presented in this paper. The grid refinement slightly reduced the grid sensitivity of the solutions, but overall the new results are fundamentally similar to the results from the earlier grids. The current grid sizes (coarse, medium, fine, and extra-fine) were 12.3, 39.1, 160.8, and 356.6 million points, respectively. Although not shown here, the results from the fine and extra-fine grids were very close, so only results from the fine grid will be shown as a representative CFD solution.

4.0   RESULTS

Over the course of the CFD validation experiment, LDV profile measurements were made in the trailing-edge corner-flow region of the wing-fuselage junction for three model configurations: the F6 wing at a model pitch angle of $5°$, the F6 wing with leading-edge extension at a model pitch angle of $-2.5°$, and the F6 wing with leading-edge extension at a model pitch angle of $5°$. All of the profile measurements were made on the port side of the model and the chord Reynolds number was held constant at 2.4×10^6. In this section, we present sample profiles for the F6 wing with leading-edge extension at a model pitch angle of $\alpha = 5°$. Sample profiles for the other model configurations can be found in Kegerise and Neuhart [5].

The velocity profiles were acquired by traversing in the z direction, up from the wing surface, for a range of (x, y) locations. The probe optical axis was tilted downward by $10°$ in the y–z plane for these measurements so that the measurement volume could be placed closer to the wing surface without clipping some of the probe beams. Each profile typically contains 28 z locations, starting at 500 μm from the wing surface (a z location closer to the wing surface could not be achieved due to laser flare noise). The (x, y) locations at which profile measurements were made are plotted in Fig. 6 and they are overlaid on an oil-flow visualization for a spatial reference. In this figure, the fuselage surface is located at $y = y_o = -236.1$ mm and the wing trailing edge is located at $x = 2961.9$ mm. Profile measurements were made at 45 unique (x, y) locations and an additional 19 repeat profiles measurements, distributed over these locations, were made to characterize the run-to-run repeatability and to help assess the measurement uncertainties.

Consider the chordwise evolution of the corner flow as we move in the downstream direction. As the trailing edge region of the wing is approached, the corner flow is exposed to an adverse pressure gradient and the convex curvature of the wing surface, both of which act to modify the mean flow and Reynolds stresses in the corner region. Given the low momentum of the fluid in the corner, where the fuselage and wing boundary layers are merged, the corner-flow eventually separates and forms an open separated flow region that extends to the wing trailing edge. The footprint of this separated flow is clearly visible in the oil-flow visualization shown in Fig. 6 and it starts at approximately $x = 2852.6$ mm and expands outboard as we move downstream toward the trailing edge.
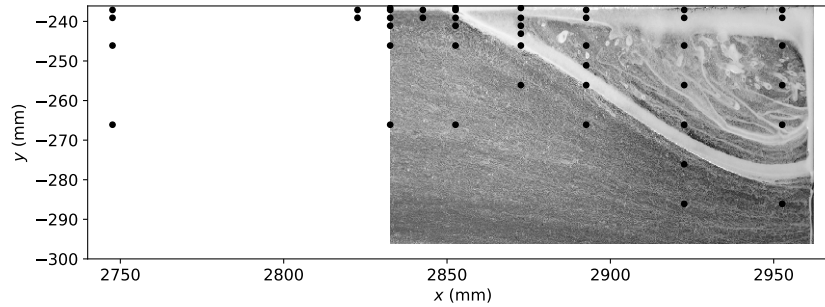
Figure 6: Locations of z-direction LDV surveys in the corner-flow region of the F6 wing with leading-edge extension. The black circles denote the (x, y)-locations of the profiles and those locations are superimposed on an image of the oil-flow visualization at $\alpha = 5°$.

Figure 7 shows the chordwise evolution of the mean velocity profiles at $y = -239.1$ mm (or $y_o - y = 3$ mm from the fuselage surface), which is deep within the fuselage boundary layer. Here, z_o in the ordinate label denotes the z location of the wing surface and uncertainty bars were excluded from the plots for clarity. As we move downstream, there is a progressive decrease in the $\overline{u}$ velocity, due to the adverse pressure gradient as well as the growth of the fuselage boundary layer. After the flow separates in the corner, we observe regions of the $\overline{u}$ profile where the velocity is negative, and therefore, the flow is moving upstream in the mean. The $\overline{w}$ velocity component ahead of separation is negative throughout the profile as the flow is moving downward, following along the convex curvature of the wing surface. Inside the separated flow, however, there are regions where the $\overline{w}$ velocity component is positive, again due to the flow moving upstream in the mean. For x locations upstream of the separation, both the $\overline{u}$ and $\overline{w}$ velocity profiles display a deficit and inflection point near 5–6 mm from the wing surface. The corresponding $\overline{v}$ velocity profiles in this region display a weak secondary flow, with flow toward the fuselage ($+\overline{v}$) below the inflection point and flow away from the fuselage ($-\overline{v}$) above the inflection point. This transverse flow suggest the presence of a vortex that lifts low momentum fluid near the wall to create the deficit in the $\overline{u}$ and $\overline{w}$ velocity profiles. While the exact origin of this vortical flow in the corner region is uncertain on the basis of the flowfield measurements we currently have, it may be a stress-induced vortex, whereby the secondary flow is induced by Reynolds shear stress gradients normal to the corner bisector. This particular mechanism for the initiation of secondary flow in the turbulent flow along a corner was studied experimentally by Gessner [18].

Figure 8 shows the chordwise evolution of the Reynolds normal stress and turbulent kinetic energy profiles at $y = -239.1$ mm. The general shapes of the normal-stress profiles are similar, but the $\overline{u'u'}$ component has the largest amplitude, followed by the $\overline{w'w'}$ component, and then the $\overline{v'v'}$ component. Upstream of the corner separation, the normal-stress and turbulent kinetic energy profiles display only modest changes as the separated flow is approached. For profile locations inside the separated flow, there is substantial growth in the normal stresses and turbulent kinetic energy and a peak develops near the inflection points in the $\overline{u}$ and $\overline{w}$ velocity profiles. The chordwise evolution of the Reynolds shear stress profiles at $y = -239.1$ mm is shown in Fig. 9. As with the normal-stress profiles, the shear stress profiles display modest changes up to where separation begins. For profiles inside the separated flow, the $\overline{u'w'}$ component has the largest amplitude due to the large $\overline{u}$ and $\overline{w}$ gradients in the z direction at this y location.

In Fig. 10, the chordwise evolution of the mean velocity profiles at $y = -266.1$ mm (or $y_o - y = 30$ mm from the fuselage surface) is shown. This y location is essentially outside of the fuselage boundary layer and

**Turbulence Measurements on a Wing-Fuselage Junction Model
for CFD Validation**

(a) $\overline{u}$ component of velocity.

(b) $\overline{v}$ component of velocity.
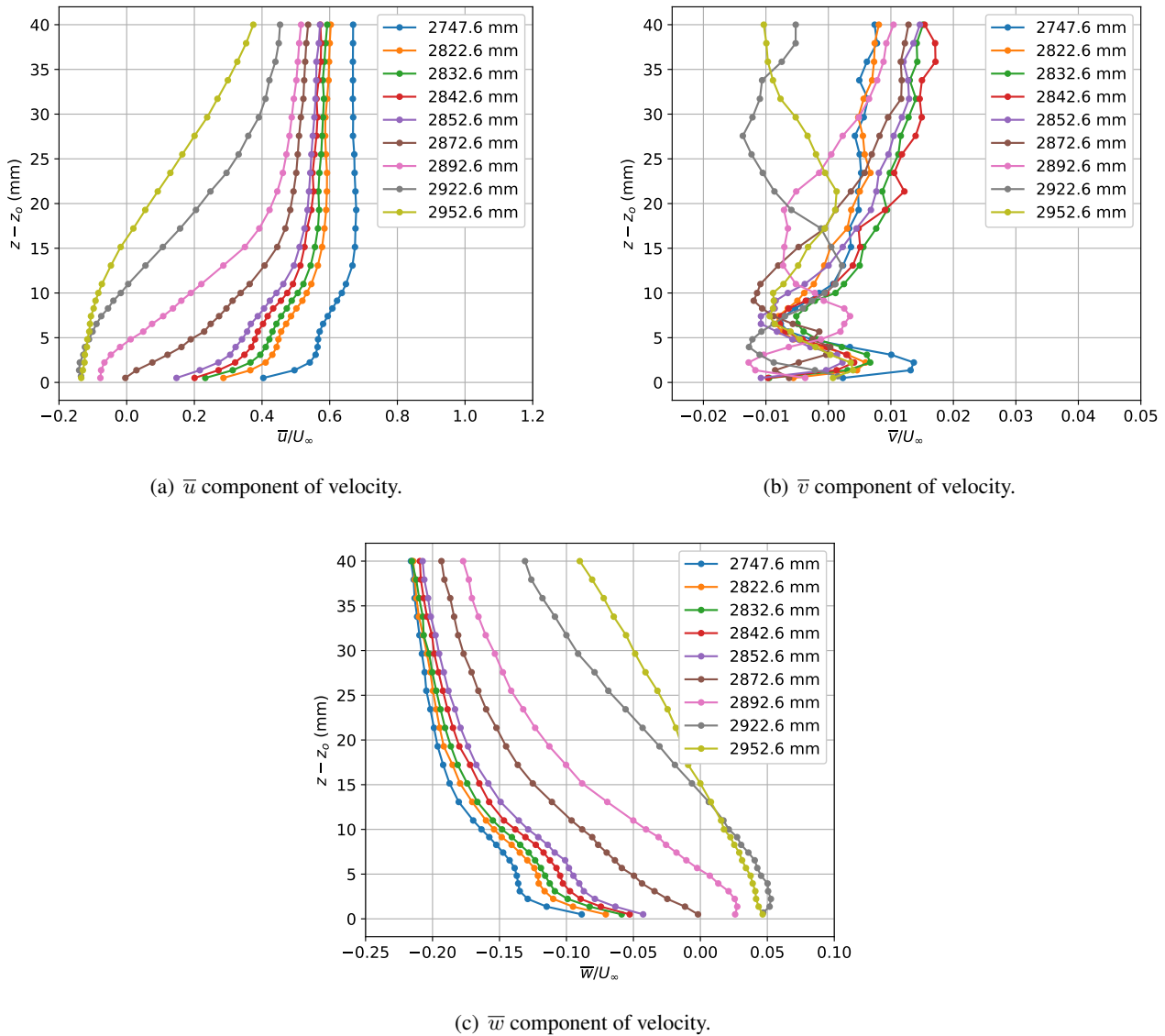

(c) $\overline{w}$ component of velocity.

Figure 7: Mean-velocity profiles in the corner-flow region of the F6 wing with leading-edge extension at $y = -239.1$ mm and several x locations. The model pitch angle was $\alpha = 5°$.

the mean profiles are indicative of the wing boundary layer. As with the $y = -239.1$ mm case, the $\overline{u}$ velocity profiles display a progressive decrease as we move downstream due to the adverse pressure gradient. Also, the $\overline{w}$ profiles display negative values throughout as the flow moves downward along the curvature of the wing surface. Upstream of the separation, the $\overline{v}$ velocity component is near zero as the freestream is approached, but as we move down toward the wing surface, $\overline{v}$ becomes increasingly negative, indicating flow outboard and away from the fuselage. In fact, as we move closer to the separated flow region, $\overline{v}$ becomes progressively more negative due to the upstream influence of the expanding separated flow region. In contrast, the $\overline{v}$ velocity profiles inside the separated flow region become less negative as we move downstream where the recirculating flow begins to turn inboard as the wing trailing edge is approached. That characteristic can be observed in the

(a) $\overline{u'u'}$ component of normal stress.

(b) $\overline{v'v'}$ component of normal stress.

(c) $\overline{w'w'}$ component of normal stress.
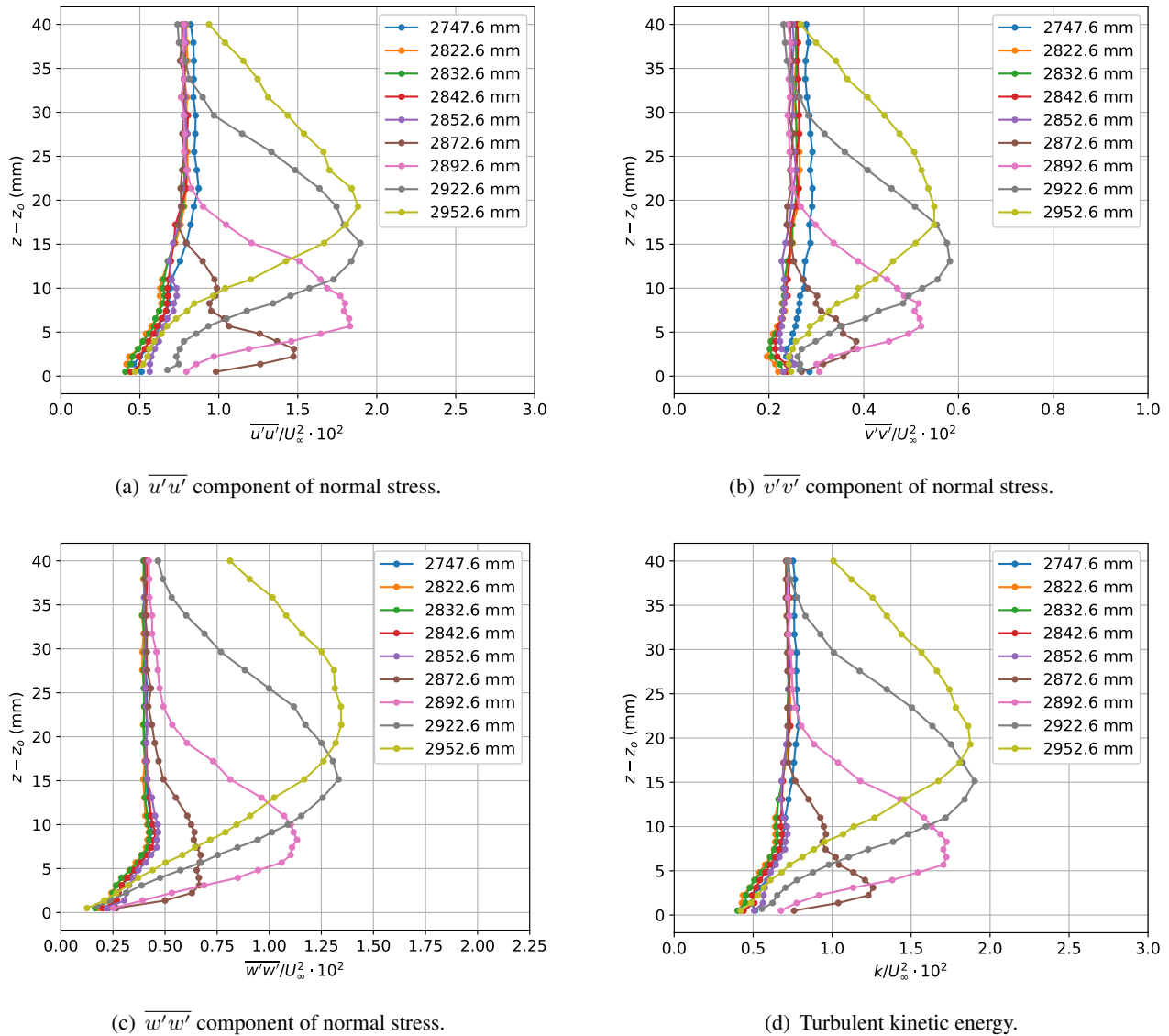

(d) Turbulent kinetic energy.

Figure 8: Normal stress and turbulent kinetic energy profiles in the corner-flow region of the F6 wing with leading-edge extension at $y = -239.1$ mm and several x locations. The model pitch angle was $\alpha = 5°$.

flow topology revealed by the oil-flow visualization shown in Fig. 6.

The chordwise evolution of the Reynolds normal stress and turbulent kinetic energy profiles at $y = -266.1$ mm is shown in Fig. 11. For x locations upstream of separation, all of the normal stress components and the turbulent kinetic energy display a modest increase as the separated flow region is approached. For profiles inside the separated flow region, the normal stresses and turbulent kinetic energy display substantial growth with downstream position. Finally, the chordwise evolution of the Reynolds shear stress profiles at $y = -266.1$ mm is shown in Fig. 12. As with the previous case, the $\overline{u'w'}$ component of shear stress displays the largest amplitude due to the large $\overline{u}$ and $\overline{w}$ gradients in the z direction. The other two shear-stress components, $\overline{u'v'}$ and $\overline{v'w'}$, are small and near zero, except in the separated flow region.

(a) $\overline{u'v'}$ component of shear stress.

(b) $\overline{u'w'}$ component of shear stress.

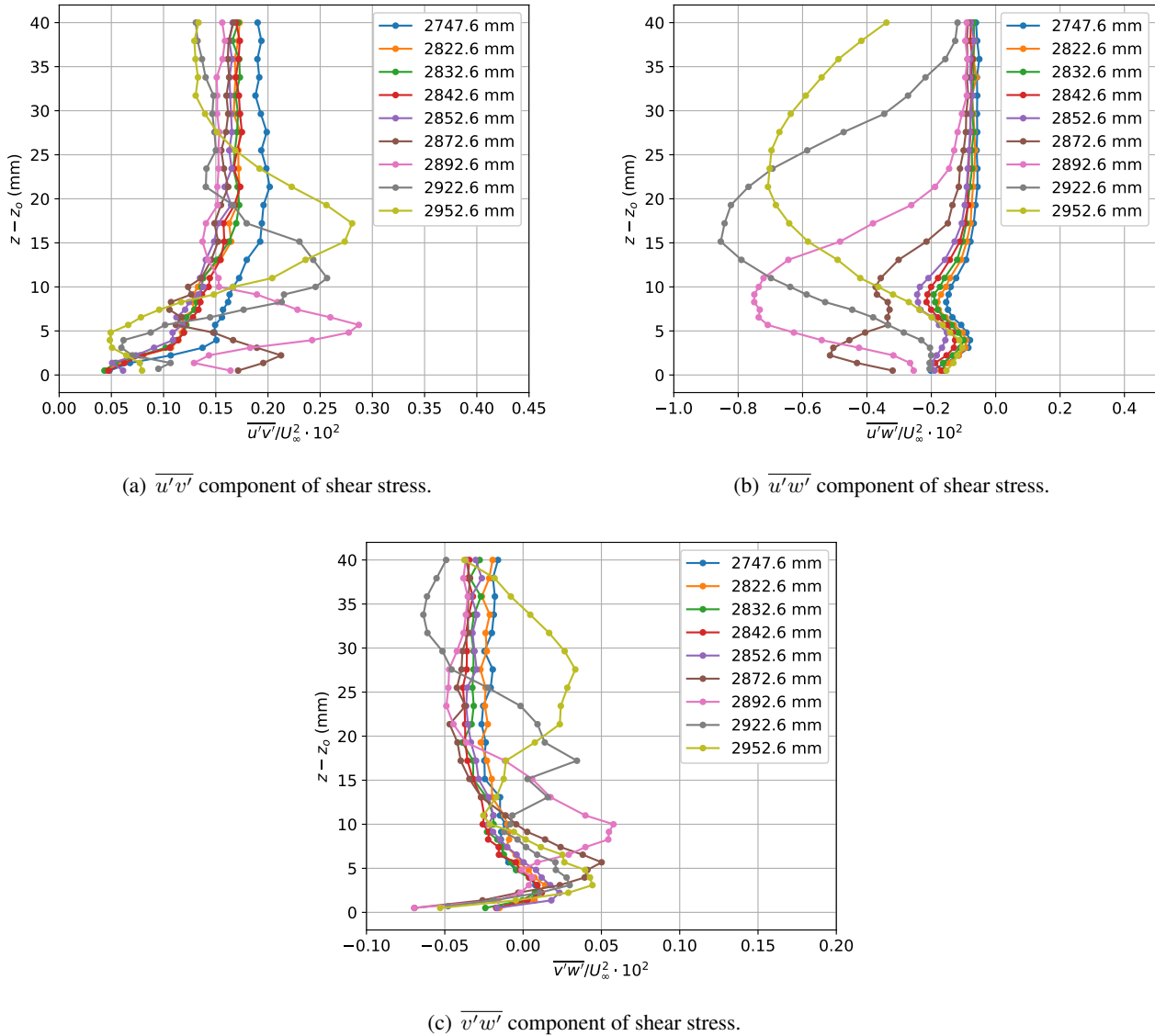

(c) $\overline{v'w'}$ component of shear stress.

Figure 9: Shear stress profiles in the corner-flow region of the F6 wing with leading-edge extension at $y = -239.1$ mm and several x locations. The model pitch angle was $\alpha = 5°$.

The oil-flow visualizations and the profiles of the velocity statistical moments may give the impression that the corner-flow separation in the wing-fuselage junction is stationary with recirculating flow inside. However, recent PIV measurements in the wing-fuselage junction by Jenkins *et al.* [19] indicate that the flow separation is nonstationary and highly unsteady. Contours of the instantaneous u velocity in an x–z plane at $y = -241.1$ mm revealed that the region of reversed or low-velocity flow in the corner separation is not fixed at one location, but instead grows and shrinks in the z direction and elongates and contracts in the x direction. This nonstationary behavior is also revealed in the histograms of the instantaneous velocity components measured with the LDV system. Consider, for example, the contour plots of the histograms for the instantaneous u and w velocity components at $x = 2892.6$ mm and $y = -239.1$ mm shown in Fig. 13. Here, the histograms for each height,

(a) $\overline{u}$ component of velocity.

(b) $\overline{v}$ component of velocity.

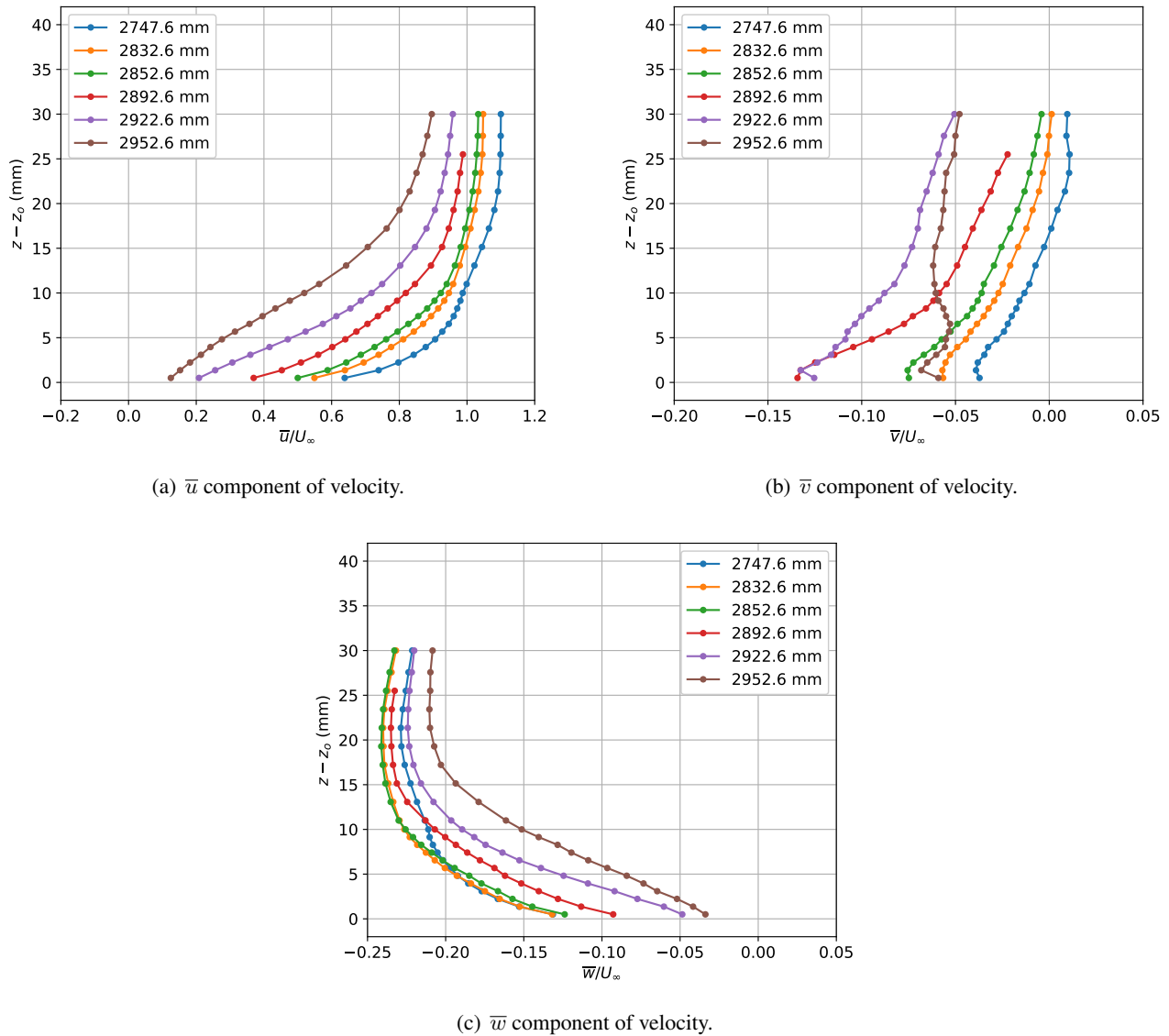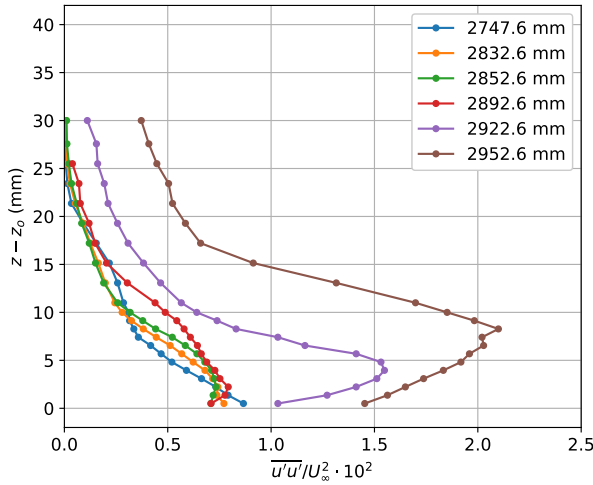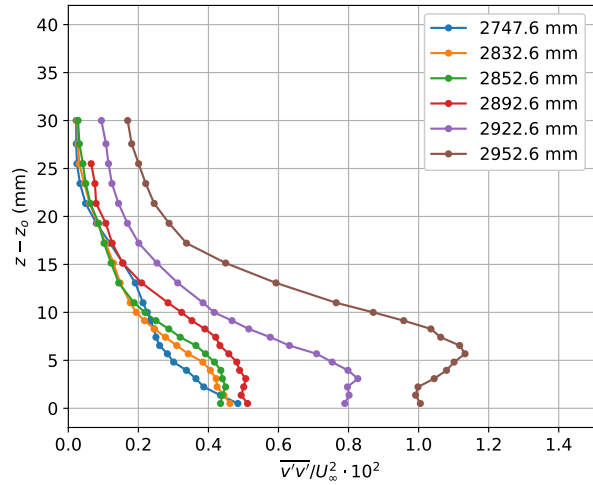(c) $\overline{w}$ component of velocity.

Figure 10: Mean-velocity profiles in the corner-flow region of the F6 wing with leading-edge extension at $y = -266.1$ mm and several x locations. The model pitch angle was $\alpha = 5°$.

$z - z_o$, in the profile were stacked together to create the contour plot and the colors represent the amplitude of the histogram. The black circle symbols denote the mean values of the velocity components at each height in the profile. In the upper portion of the profiles, where we are above the separated corner flow at this (x, y) location and inside the fuselage boundary layer, the histograms are nearly Gaussian and centered on the mean values of velocity. However, in the lower portion of the profiles, the histograms display a bimodal distribution, indicating that the flow is at times reversed and moving upstream (u negative, w positive) and at other times attached and moving downstream (u positive, w negative). This is consistent with the unsteady motion of the separated flow as revealed by the PIV measurements. Histograms for the instantaneous v velocity component (not shown here) did not have a bimodal distribution, but instead, they were nearly Gaussian with a mean value
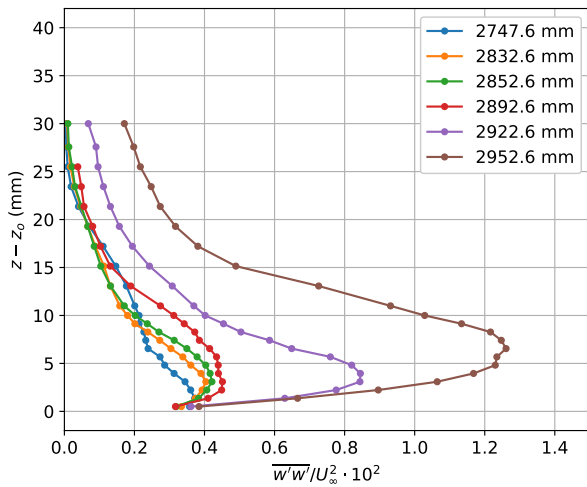
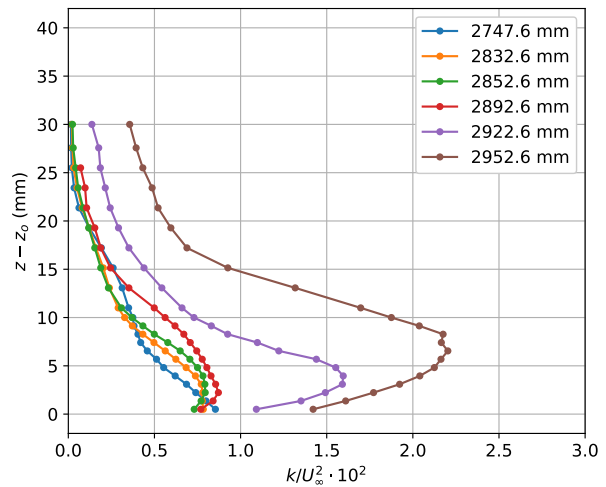**Turbulence Measurements on a Wing-Fuselage Junction Model for CFD Validation**

(a) $\overline{u'u'}$ component of normal stress.

(b) $\overline{v'v'}$ component of normal stress.

(c) $\overline{w'w'}$ component of normal stress.

(d) Turbulent kinetic energy.

Figure 11: Normal stress and turbulent kinetic energy profiles in the corner-flow region of the F6 wing with leading-edge extension at $y = -266.1$ mm and several x locations. The model pitch angle was $\alpha = 5°$.

near zero. Other locations in the separated flow, particularly for y locations near the fuselage surface, revealed similar bimodal histograms for the u and w velocity components.

In the remainder of this section, we present comparisons between the experimental results and representative computations. The main intent here is to highlight some of the discrepancies that exist between the experimental measurements and a sample CFD computation that uses state-of-the-art turbulence models. It is not an exhaustive survey of the differences, and computations of our test case are still ongoing at this time. Figure 14 compares the oil-flow visualization of the separated corner flow with the computed surface streamlines for two Spalart-Allmaras one-equation turbulence models [20]: SA-RC-QCR2000 (with rotation/curvature correction and quadratic constitutive relation) [21] and SA-RC (with rotation/curvature correction) [22]. Here the
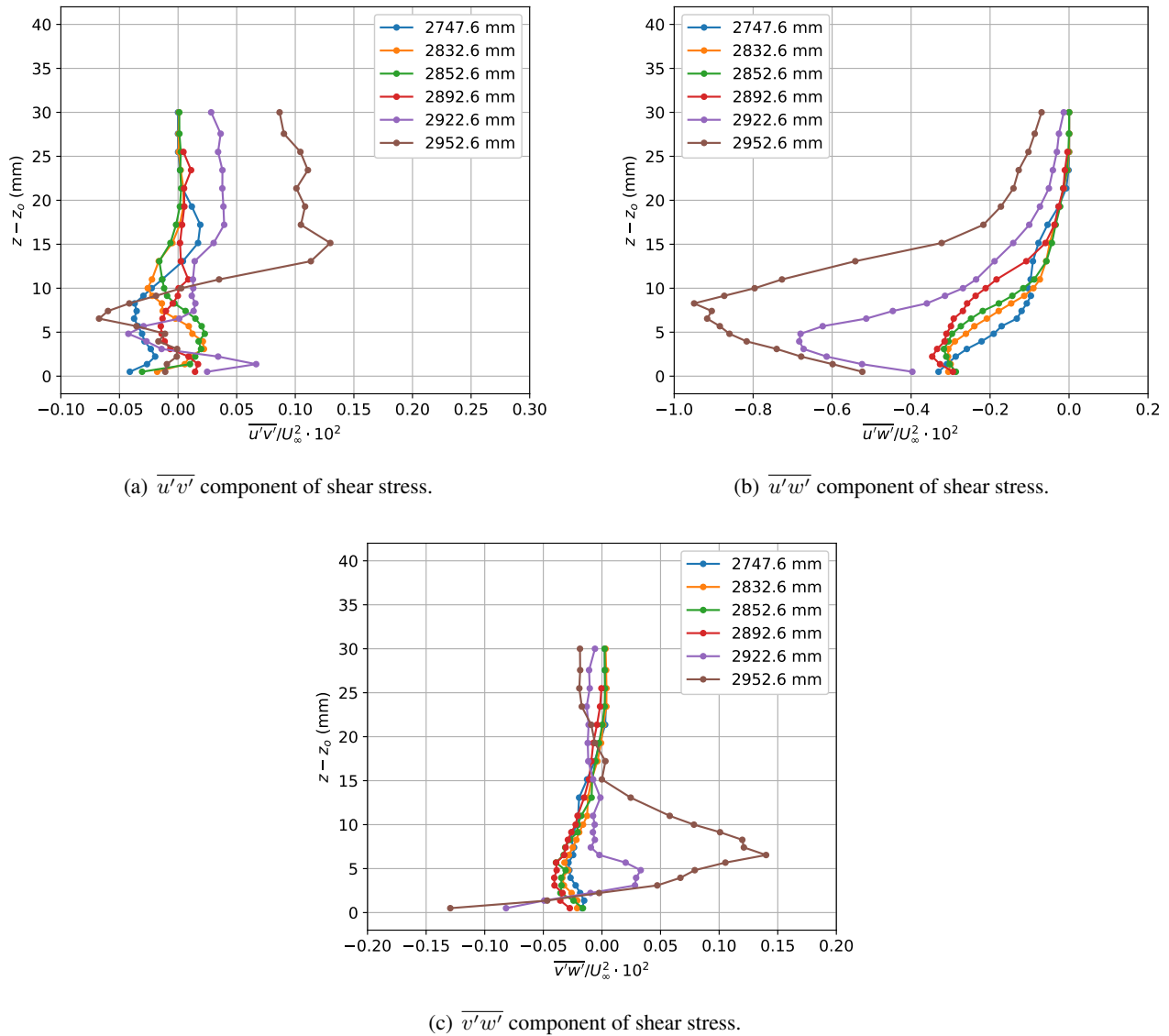
(a) $\overline{u'v'}$ component of shear stress.

(b) $\overline{u'w'}$ component of shear stress.

(c) $\overline{v'w'}$ component of shear stress.

Figure 12: Shear stress profiles in the corner-flow region of the F6 wing with leading-edge extension at $y = -266.1$ mm and several x locations. The model pitch angle was $\alpha = 5°$.

model pitch angle was $\alpha = 5°$. A plot of the separation size versus pitch angle is also shown (Fig. 14d) and this compares the experimentally determined separation length, ℓ, and width, w, to the computed values for the two turbulence models. The uncertainty bars on the experimental data represent the 95% confidence intervals for the length and width measurements.

In a qualitative sense, the SA-RC-QCR2000 model more closely matches the surface topology of the separated corner flow as revealed by the oil-flow visualization than does the SA-RC model. This is consistent with previous studies that have shown that QCR helps models like SA-RC perform better in corner flows [23, 24]. The predicted separation width for the SA-RC-QCR2000 model is observed to match the measured width to within the experimental uncertainty. However, this model also overpredicts the separation length by 10–20%.

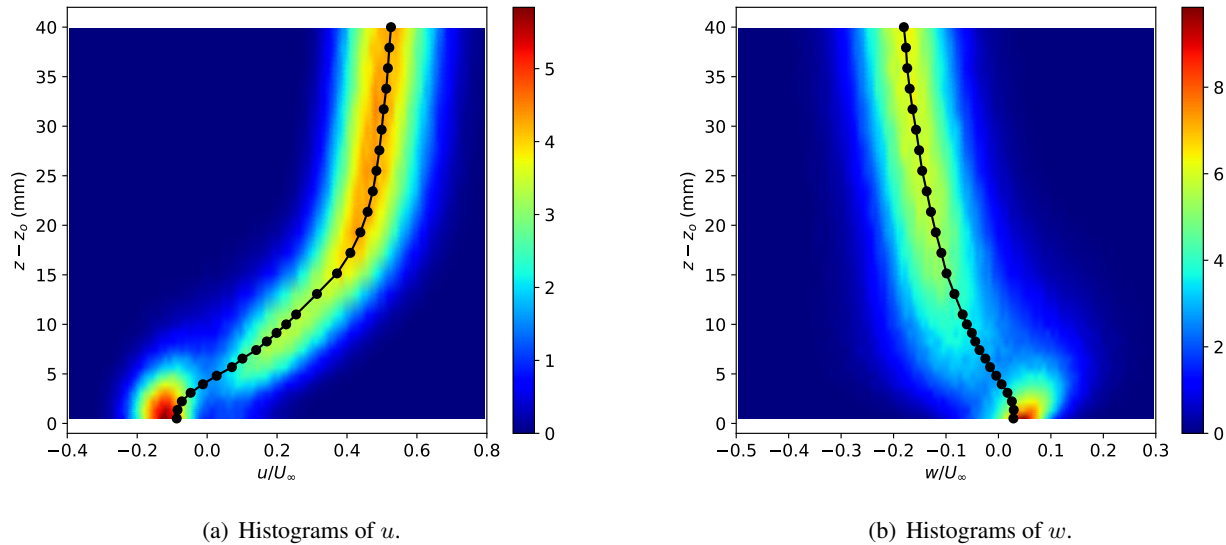**Turbulence Measurements on a Wing-Fuselage Junction Model
for CFD Validation**

(a) Histograms of u.

(b) Histograms of w.

Figure 13: Contour plots of the histograms for the instantaneous u and w velocity components at x = 2892.6 mm and y = −239.1 mm. The circle symbols in the plots denote the mean values of the velocity components.

The SA-RC model is seen to overpredict both the separation length and width over the range of pitch angles considered.

In Figs. 15, 16, and 17, experimentally measured mean velocity and Reynolds-stress profiles at three locations in the corner-flow region are compared to profiles predicted with the SA-RC-QCR2000 turbulence model. In Fig. 15 ($x = 2747.6$ mm, $y = −237.1$ mm) the measurement location was approximately one separation length upstream and deep within the fuselage boundary layer. Here, the $\overline{v}$ and $\overline{w}$ components are fairly well predicted, but the $\overline{u}$ is overpredicted. The $\overline{v'v'}$ and $\overline{w'w'}$ normal stresses are also fairly well predicted, but the $\overline{u'u'}$ is severely underpredicted. The Reynolds shear stress components $\overline{u'v'}$ and $\overline{v'w'}$ are well predicted at this location. In contrast, the predicted and measured $\overline{u'w'}$ component is significantly different in terms of the magnitude, but there are qualitative similarities in the profiles.

In Fig. 16 ($x = 2852.6$ mm, $y = −237.1$ mm) the measurement location was near the beginning of the corner separation, in the mean, as determined from the experiment. However, the predicted flowfield has separated upstream of this location and as such, the experimentally measured mean velocity and Reynolds-stress profiles display significant differences when compared to the predicted profiles. Finally, Fig. 17 ($x = 2892.6$ mm, $y = −246.1$ mm) shows mean velocities and Reynolds-stress profiles at a location well into the separated flow region and here as well, there are significant discrepancies between the experimentally measured and predicted profiles.

5.0   CONCLUSIONS AND FUTURE WORK

In this paper, we have presented turbulence measurements on a full-span wing-fuselage junction model that were part of a larger CFD validation experiment. The model geometry—which was designed in coordination with CFD subject matter experts from government, industry, and academia—exhibits a separated corner-flow region near the wing trailing edge that current RANS turbulence models are unable to reliably predict. The ultimate goal of this experimental effort is to provide a publicly-available high-quality flowfield and surface data set with quantified boundary conditions, geometry, and measurement uncertainties. It is expected that this
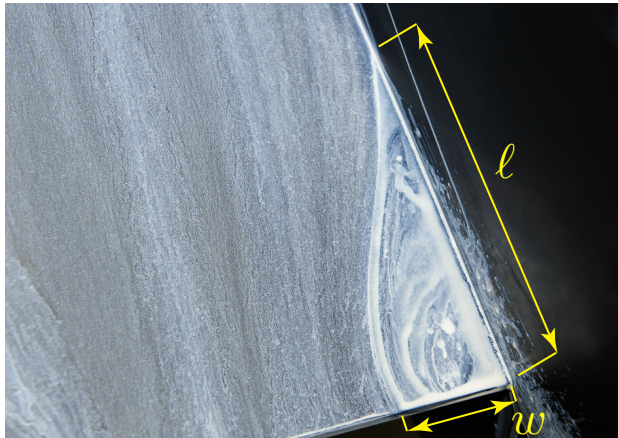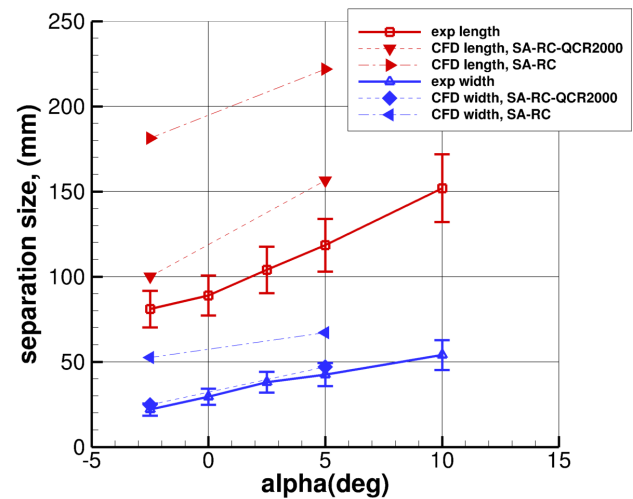
(a) Oil-flow visualization at $\alpha = 5°$.
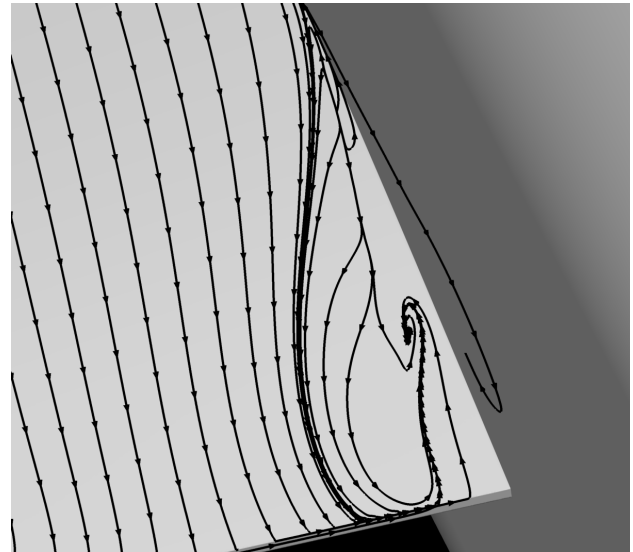
(b) Computed surface streamlines at $\alpha = 5°$ with turbulence model SA-RC-QCR2000.
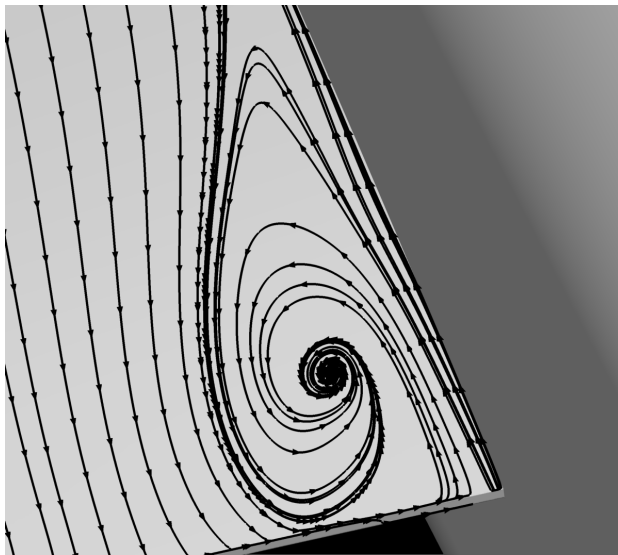
(c) Computed surface streamlines at $\alpha = 5°$ with turbulence model SA-RC.

(d) Corner separation length and width.

Figure 14: Comparison of experimental and computed corner flow separation size for the F6 wing with leading-edge extension at $\alpha = 5°$.

data set will be suitable for use in CFD workshop environments and will help CFD practitioners validate and improve their predictive capabilities for turbulent separated corner flows.

A laser Doppler velocimetry (LDV) system—mounted within the test model—was used to perform flowfield measurements near the trailing edge of the wing-fuselage junction. In this corner region, profile measurements were made upstream of the corner-flow separation, near the beginning of separation, and within the separated-flow region. All three components of the mean velocity, all six components of the Reynolds-stress tensor, and

Turbulence Measurements on a Wing-Fuselage Junction Model for CFD Validation

(a) Mean velocity profiles.

(b) Reynolds normal stress profiles.
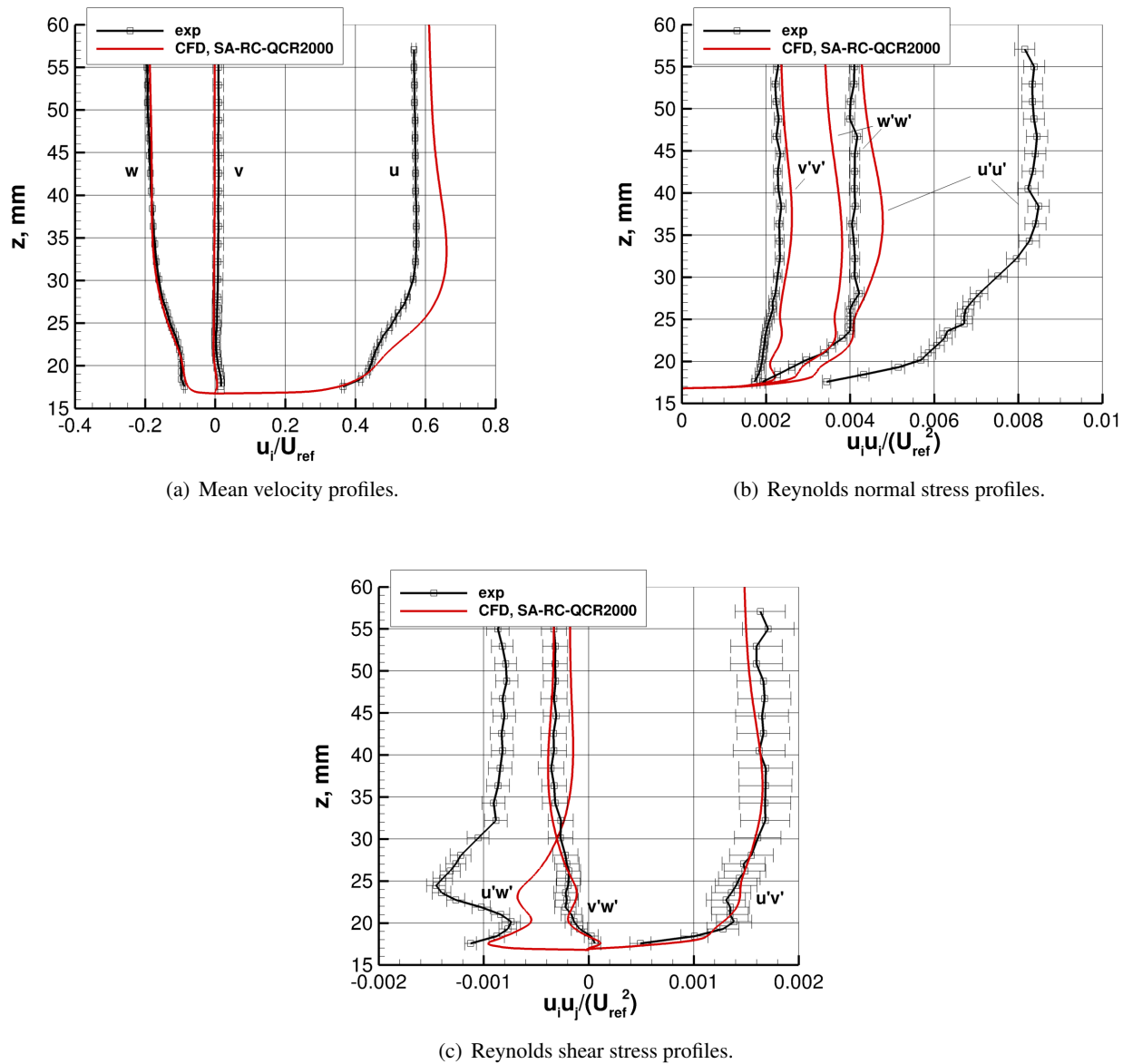

(c) Reynolds shear stress profiles.

Figure 15: Comparisons of the experimental and computed (with SA-RC-QCR2000) mean velocity and Reynolds-stress profiles at $x = 2747.6$ mm, $y = -237.1$ mm, and $\alpha = 5°$.

the turbulent kinetic energy were calculated from the LDV measurements. Sample profiles of these turbulent-flow quantities were presented and the general features associated with them were discussed. Histograms of the instantaneous velocity components were also calculated and they suggest that the corner-flow separation is highly nonstationary and exhibits bi-modal characteristics in the main-flow direction. Finally, a comparison between the experimental measurements and representative CFD using state-of-the-art turbulence models was made. In a qualitative sense, the computed surface streamlines are similar to the surface topology of the corner separation as revealed by oil-flow visualizations. However, the computations predicted that the corner separation begins upstream of where it occurs in the experiment, in the mean. In comparing the experimental

(a) Mean velocity profiles.

(b) Reynolds normal stress profiles.
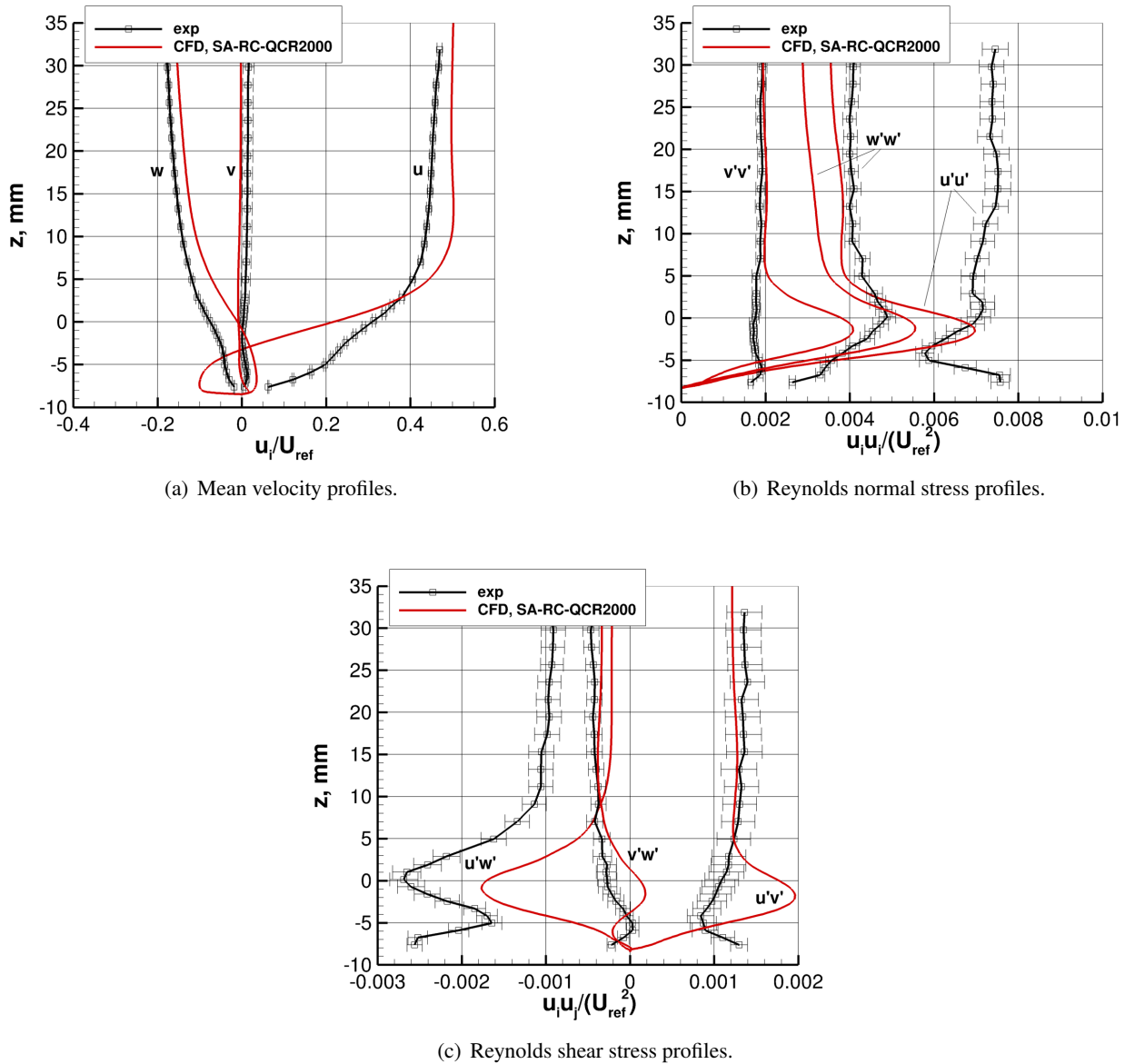

(c) Reynolds shear stress profiles.

Figure 16: Comparisons of the experimental and computed (with SA-RC-QCR2000) mean velocity and Reynolds-stress profiles at $x = 2852.6$ mm, $y = -237.1$ mm, and $\alpha = 5°$.

and computed mean velocity and Reynolds-stress profiles, there were discrepancies between some of the components at a spatial location well upstream of the separated flow. However, at the beginning of separation and within the separated-flow region, there were large differences between all of the components—a results that is not too surprising given that the predicted location of separation is not correct.

A second test entry with the junction model is scheduled for early 2020 and there, additional flowfield measurements with the LDV system will be made to augment the existing database. Flowfield measurements will also be made with particle image velocimetry (PIV) and it is expected that the PIV measurements will help identify regions of interest in the flowfield where more detailed LDV profiles can be acquired.

(a) Mean velocity profiles.

(b) Reynolds normal stress profiles.
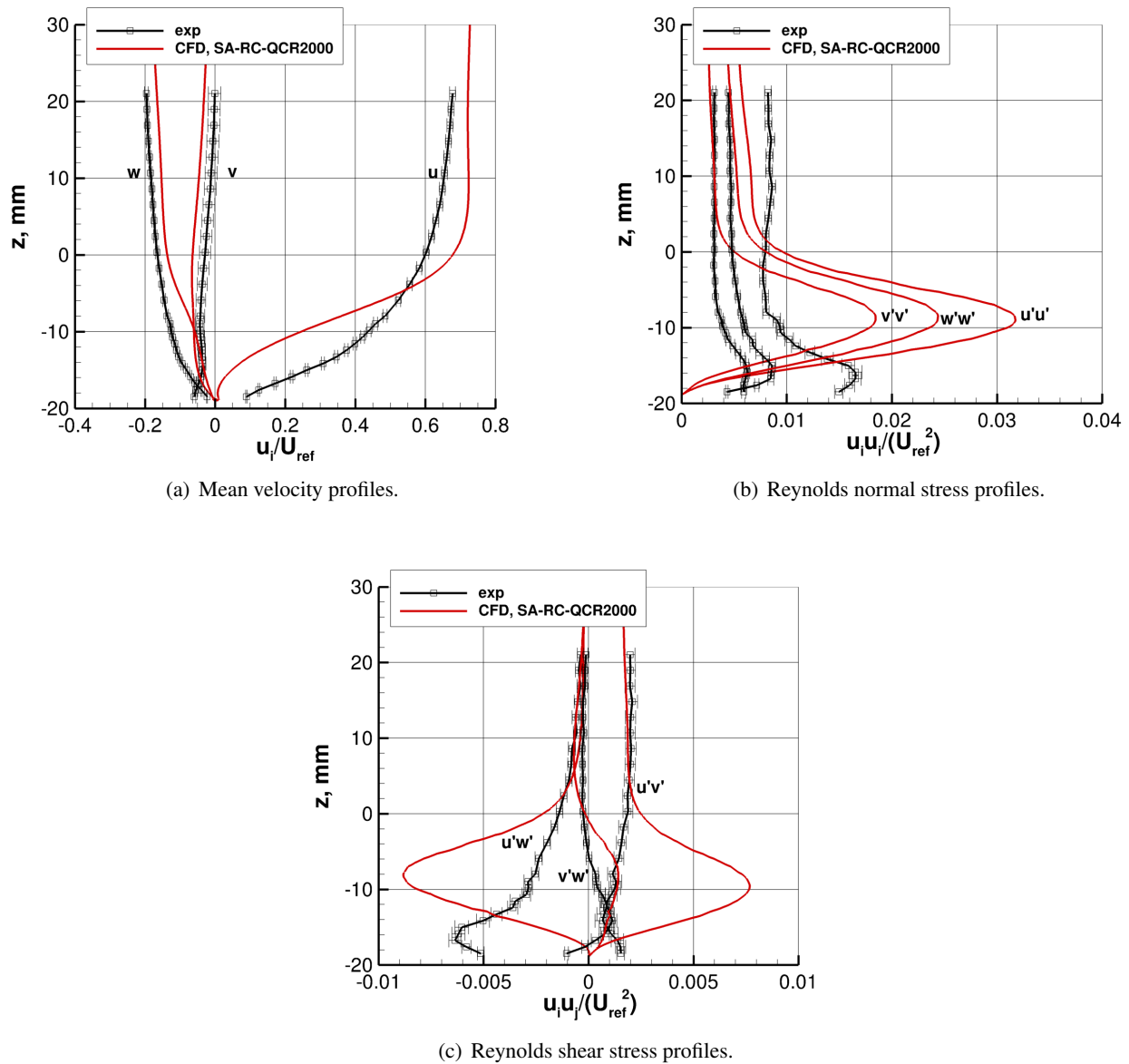

(c) Reynolds shear stress profiles.

Figure 17: Comparisons of the experimental and computed (with SA-RC-QCR2000) mean velocity and Reynolds-stress profiles at $x = 2892.6$ mm, $y = -246.1$ mm, and $\alpha = 5°$.

REFERENCES

[1] Vassberg, J. C., Tinoco, E. N., Mani, M., Brodersen, O. P., Eisfeld, B., Wahls, R. A., Morrison, J. H., Zickuhr, T., Laflin, K. R., and Mavriplis, D. J., "Abridged Summary of the Third AIAA Computational Fluid Dynamics Drag Prediction Workshop," *Journal of Aircraft*, Vol. 45, No. 3, May–June 2008, pp. 781–798.

[2] Rumsey, C. L., Neuhart, D. H., and Kegerise, M. A., "The NASA Juncture Flow Experiment: Goals,

Progress, and Preliminary Testing (Invited)," AIAA Paper 2016-1557, January 2016.

[3] Rumsey, C. L. and Morrison, J. H., "Goals and Status of the NASA Juncture Flow Experiment," AVT Specialists Meeting on Progress and Challenges in Validation Testing for CFD, STO-MP-AVT-246-03, September 2016.

[4] Kegerise, M. A., Neuhart, D. H., Hannon, J. A., and Rumsey, C. L., "An Experimental Investigation of a Wing-Fuselage Junction Model in the NASA Langley 14- by 22-Foot Subsonic Wind Tunnel," AIAA Paper 2019-0077, January 2019.

[5] Kegerise, M. A. and Neuhart, D. H., "An Experimental Investigation of a Wing-Fuselage Junction Model in the NASA Langley 14- by 22-Foot Subsonic Tunnel," NASA TM 220286, June 2019.

[6] Neuhart, D. H. and McGinley, C. B., "Free-Stream Turbulence Intensity in the Langley 14- by 22-Foot Subsonic Tunnel," NASA TP 213247, 2004.

[7] Gentry, G. L., Quinto, F. P., Gatlin, G. G., and Applin, Z. T., "The Langley 14- by 22-Foot Subsonic Tunnel," NASA TP 3008, 1990.

[8] Lowe, K. T., *Design and Application of a Novel Laser-Doppler Velocimeter for Turbulence Structural Measurements in Turbulent Boundary Layers*, Ph.D. thesis, Virginia Polytechnic Institute and State University, 2006.

[9] Ölçmen, S. M. and Simpson, R. L., "An Experimental Study of a Three-Dimensional Pressure-Driven Turbulent Boundary Layer," *Journal of Fluid Mechanics*, Vol. 290, 1995, pp. 225–262.

[10] Albrecht, H. E., Borys, M., Damaschke, N., and Tropea, C., *Laser Doppler and Phase Doppler Measurement Techniques*, Springer, Berlin, Germany, 2003.

[11] Coleman, H. W. and Steele, W. G., *Experimentation and Uncertainty Analysis for Engineers*, Wiley Interscience, New York, NY, 1999.

[12] Benedict, L. H. and Gould, R. D., "Towards Better Uncertainty Estimates for Turbulence Statistics," *Experiments in Fluids*, Vol. 22, 1996, pp. 129–136.

[13] Anderson, W. and Bonhaus, D., "An Implicit Upwind Algorithm for Computing Turbulent Flows on Unstructured Grids," *Computers and Fluids*, Vol. 23, No. 1, 1994, pp. 1–22.

[14] Anderson, W., Rausch, R., and Bonhaus, D. L., "Implicit/Multigrid Algorithms for Incompressible Turbulent Flows on Unstructured Grids," *Journal of Computational Physics*, Vol. 128, 1996, pp. 391–408.

[15] Roe, P. L., "Characteristic-Based Schemes for Euler Equations," *Annual Review of Fluid Mechanics*, Vol. 18, 1986, pp. 337–365.

[16] Lee, H. C. and Pulliam, T. H., "OVERFLOW Juncture Flow Computations Compared with Experimental Data," AIAA Paper 2019–0080, January 2019.

[17] Rumsey, C. L., Carlson, J. R., and Ahmad, N. N., "FUN3D Juncture Flow Computations Compared with Experimental Data," AIAA Paper 2019–0079, January 2019.

[18] Gessner, F. B., "The Origin of Secondary Flow in Turbulent Flow along a Corner," *Journal of Fluid Mechanics*, Vol. 58, No. 1, 1973, pp. 1–25.

[19] Jenkins, L. N., Yao, C. S., and Bartram, S. M., "Flow-Field Measurements in a Wing-Fuselage Junction Using an Embedded Particle Image Velocimetry System," AIAA Paper 2019-0078, January 2019.

[20] Spalart, P. R. and Allmaras, S. R., "A One-Equation Turbulence Model for Aerodynamic Flows," *Recherche Aerospatiale*, Vol. 1, 1994, pp. 5–21.

[21] Spalart, P. R., "Strategies for Turbulence Modelling and Simulation," *International Journal of Heat and Fluid Flow*, Vol. 21, 2000, pp. 252–263.

[22] Shur, M. L., Strelets, M. K., Travin, A. K., and Spalart, P. R., "Turbulence Modeling in Rotating and Curved Channels: Assessing the Spalart-Shur Correction," *AIAA Journal*, Vol. 38, No. 5, 2000, pp. 784–792.

[23] Yamamoto, K., Tanaka, K., and Murayama, M., "Comparison Study of Drag Prediction for the 4th CFD Drag Prediction Workshop using Structured and Unstructured Mesh Methods," AIAA Paper 2010-4222, June–July 2010.

[24] Bordji, M., Gand, F., Deck, S., and Brunet, V., "Investigation of a Nonlinear Reynolds-Averaged Navier-Stokes Closure for Corner Flows," *AIAA Journal*, Vol. 54, No. 2, 2016, pp. 386–398.